Ultrafast orbital Hall effect in metallic nanoribbons

Oliver Busch ⬤,* Franziska Ziolkowski ⬤, Börge Göbel ⬤, Ingrid Mertig ⬤, and Jürgen Henk ⬤
Institut für Physik, Martin Luther University Halle-Wittenberg, 06099 Halle, Germany

The orbital Hall effect can generate currents of angular momentum more efficiently than the spin Hall effect in most metals. However, so far, it has only been understood as a steady-state phenomenon. In this theoretical study, the orbital Hall effect is extended into the time domain. We investigate the orbital angular momenta and their currents induced by a femtosecond laser pulse in a Cu nanoribbon. Our numerical simulations provide detailed insights into the laser-driven electron dynamics on ultrashort timescales with atomic resolution. The ultrafast orbital Hall effect described in this paper is consistent with the familiar pictorial representation of the static orbital Hall effect, but we also find pronounced differences between physical quantities that carry orbital angular momentum and those that carry charge. For example, there are deviations in the time series of the respective currents. This paper lays the foundations for investigating ultrafast Hall effects in confined metallic systems.

I. INTRODUCTION

The concepts and ideas of spintronics have recently been expanded in two promising ways. First, in addition to exploiting the spin degree of freedom of electrons, their orbital degree of freedom is also used, leading to the field of orbitronics [1–3]. As a result, well-established effects such as the spin Hall [4–7] and the (spin) Edelstein effect [8–11] are complemented by their orbital counterparts, namely the orbital Hall effect (OHE) [12–16] and the orbital Edelstein effect [17–20].

Second, well-known steady-state phenomena are brought into the time domain by driving systems on the picosecond timescale (e.g., using terahertz radiation [21]) or on the femtosecond timescale (e.g., using ultrashort laser pulses [22]).

In this paper, we aim to investigate theoretically the ultrafast orbital Hall effect (UOHE) in a metallic nanoribbon, thereby reuniting these two paths. More precisely, we study the generation of the flow of orbital angular momentum (OAM) transverse to an oscillating external electric field [23,24]; this OAM flow is transient in nature, with a duration given by the laser pulse. As a result, we illuminate the interplay of laser-induced longitudinal and transversal charge currents, occupation dynamics, and accumulated OAM, as well as OAM currents on the femtosecond timescale with atomic resolution.

The steady state is commonly addressed by a conductivity tensor, often calculated within linear response theory (e.g., Refs. [7,25–27]). Such a tensor describes the relevant physics,

but lacks details on the microscopic level; for example, it does not facilitate access to spatial resolution. Approaches relying on response tensors have been successfully brought into the time (frequency) domain. Examples include spin polarization and photocurrents calculated in dependence of frequency [28–33]. However, the consideration of ultrafast transport phenomena in small samples requires a strategy that provides easy access to both spatial and temporal resolution.

We provide detailed insights into the electron dynamics that manifest themselves in the ultrafast orbital Hall effect
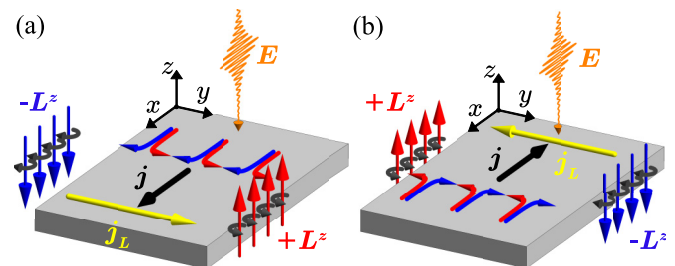

FIG. 1. Snapshots of the ultrafast orbital Hall effect in a two-dimensional sample (gray rectangular solid). (a) A linearly polarized femtosecond laser pulse impinges perpendicular to the surface (along the z axis) onto the sample. The laser's electric field E (orange), oscillating along the nanoribbon ($\pm x$ direction), causes an oscillating longitudinal charge current j, which, at the moment depicted here, is oriented in $+x$ direction (black arrow) and is deflected toward the ribbon's edges; confer the three representative pairs of current filaments (bent blue and red arrows). Hence, orbital angular momentum (OAM) L^z is transported across the ribbon, giving rise to a transverse OAM current j_L (yellow arrow along $+y$ direction). As a result, L^z is accumulated with opposite orientation at the edges (upward red and downward blue arrows). (b) Half a laser's period later, the reversal of E reverses the orientation of j, j_L, and L^z. The periodic field switching creates an ultrafast (on the femtosecond scale) orbital Hall effect.

---

*oliver.busch@physik.uni-halle.de

(sketched in Fig. 1). We achieve disentanglement of the currents and the orbital angular momenta induced by a femtosecond laser pulse in a nanoribbon [34] with respect to space and time through numerical simulations performed within our theoretical framework EVOLVE [35–38]. We show that the typical picture of the steady OHE [2,13–16] can be extended toward the femtosecond scale; it is thus appropriate for the UOHE in general. However, the rather strong perturbation of the system by the laser pulse attenuates the coherence among the involved physical quantities (depicted in Fig. 1) right after the pulse's maximum. In order to clarify these phenomena, we present spatial and temporal dependencies of the relevant physical quantities and provide animations of the dynamics in the Supplemental Material [39].

II. THEORETICAL ASPECTS

We briefly present the main ideas of our approach to ultrafast electron dynamics, based on our code EVOLVE, which is described in more detail in Appendices A–C, and elsewhere [35–38].

For the purpose of this paper, we chose a ribbon made of a Cu(001) monolayer. The free-standing film forms a square lattice, with Cartesian axes chosen as $x \equiv [110]$, $y \equiv [\bar{1}10]$, and $z \equiv [001]$ (Fig. 1). We apply periodic boundary conditions in x direction (i.e., closed circuit geometry). The ribbon is 15 atomic rows wide along y.

The electron dynamics is described by the von Neumann equation

$$-i\hbar \frac{d\hat{\rho}(t)}{dt} = [\hat{\rho}(t), \hat{H}(t)] \qquad (1)$$

for the one-particle density matrix $\hat{\rho}(t)$. The latter is either expressed in a site-orbital-spin basis or in the eigenstate basis of the Hamiltonian $\hat{H}_0$. $\hat{H}_0$ describes the electronic structure of the sample in real space; it is given in tight-binding form and includes spin-orbit coupling [40–42].

The time-dependent Hamiltonian $\hat{H}(t)$ in Eq. (1) supplements $\hat{H}_0$ by the electric field of the femtosecond laser pulse [43]. This field is a carrier wave of $\hbar\omega = 1.55$ eV energy (equivalent to a period of about $T = 2.7$ fs) with a Lorentzian envelope of 10-fs width and center at $t = 0$ fs [Fig. 2(a)]; it is linearly polarized and impinges along the z axis (Fig. 1). The laser's amplitude is chosen to obtain a fluence of about 4.3 mJ cm^{-2} and 0.4 excited electrons per site. The geometry of the entire setup (sample and laser) dictates that only the z component of the OAM $\langle \boldsymbol{L} \rangle$ is produced by the incident radiation (see Refs. [37,38,44] and the symmetry analysis in Appendix D).

Spatiotemporal properties of an observable O are obtained by taking partial traces in the expectation value $\langle O \rangle(t) = \text{tr}[\hat{\rho}(t)\,\hat{O}]$, with $\hat{\rho}(t)$ in the site-orbital-spin basis. Besides the occupation probabilities $\langle p_k \rangle(t)$ (k site index), we address currents [37,45]

$$\langle j_{kl} \rangle(t) \equiv \frac{i}{2}\langle \rho_{lk}(t)\, h_{kl}(t) \rangle - \langle l \leftrightarrow k \rangle \qquad (2)$$

from site l to site k. Here, ρ_{lk} and h_{kl} are off-diagonal blocks of the density matrix and of the Hamiltonian matrix in the site representation, respectively. Moreover, we present the z component $\langle L_k^z \rangle(t)$ of the OAM at site k and the L^z-polarized
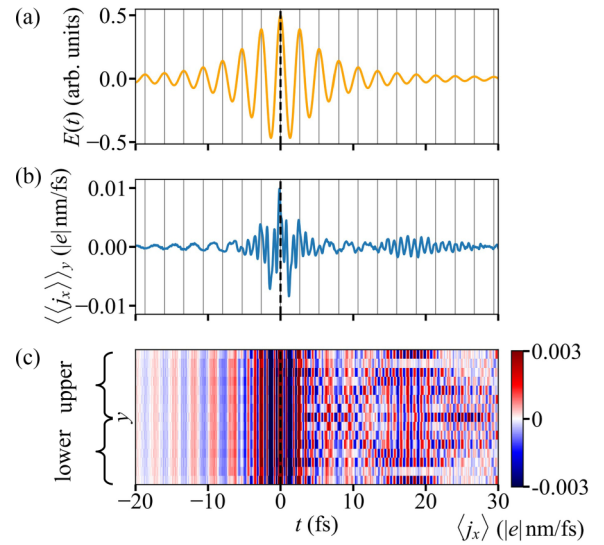

FIG. 2. Longitudinal current. (a) Amplitude of the laser pulse with a width of 10 fs and centered at $t = 0$ fs. (b) Mean longitudinal current $\langle\langle j_x \rangle\rangle_y(t)$; see text. Vertical lines mark maxima of the laser amplitude. (c) Profile of currents of x-oriented links (along the ribbon), depicted as color scale. The y average of these currents gives the data shown in panel (b).

OAM currents

$$\langle j_{kl}^z \rangle(t) \equiv \frac{1}{2}\big[\langle L_k^z j_{kl} \rangle(t) + \langle j_{kl} L_l^z \rangle(t) \big] \qquad (3)$$

from site l to site k [38]; L^z is taken with respect to the sites' positions [k and l in Eq. (3), atomic center approximation (ACA) [46,47]].

Cu exhibits a small spin Hall conductivity, which is attributed to its weak spin-orbit coupling (SOC) [48]. In contrast to the spin Hall effect (SHE), the OHE can arise without SOC [27] but requires hybridization of specific atomic orbitals (see, e.g., Refs. [2,46,49–54] for more details of the ACA). Indeed, all results presented in the following remain qualitatively the same if we neglect SOC, thereby confirming the hybridization mechanism as the origin of orbital currents. In summary, due to its small SOC, Cu is the system of choice in this paper since it exhibits a small SHE so that the OHE dominates over the SHE.

III. LASER-INDUCED LONGITUDINAL CURRENTS

The electric field of the laser drives a current along the nanoribbon (black arrow in Fig. 1). Averaging currents $\langle j_{kl} \rangle(t)$ of links $l \rightarrow k$ that are oriented in $+x$ direction [Fig. 2(c)] over the ribbon's width yields the mean longitudinal current $\langle\langle j_x \rangle\rangle_y(t)$ [Fig. 2(b); for animations of the dynamics, see the Supplemental Material [39]].

For small laser amplitudes, $\langle\langle j_x \rangle\rangle_y(t)$ is expectedly very well correlated with the laser's frequency. However, the time sequence becomes complicated at large field strengths and exhibits a long-period beating pattern (see the feature at about 18 fs), which we attribute to various timescales. First, there is the laser period. Second, the electronic structure imposes timescales via the hopping rates in the tight-binding
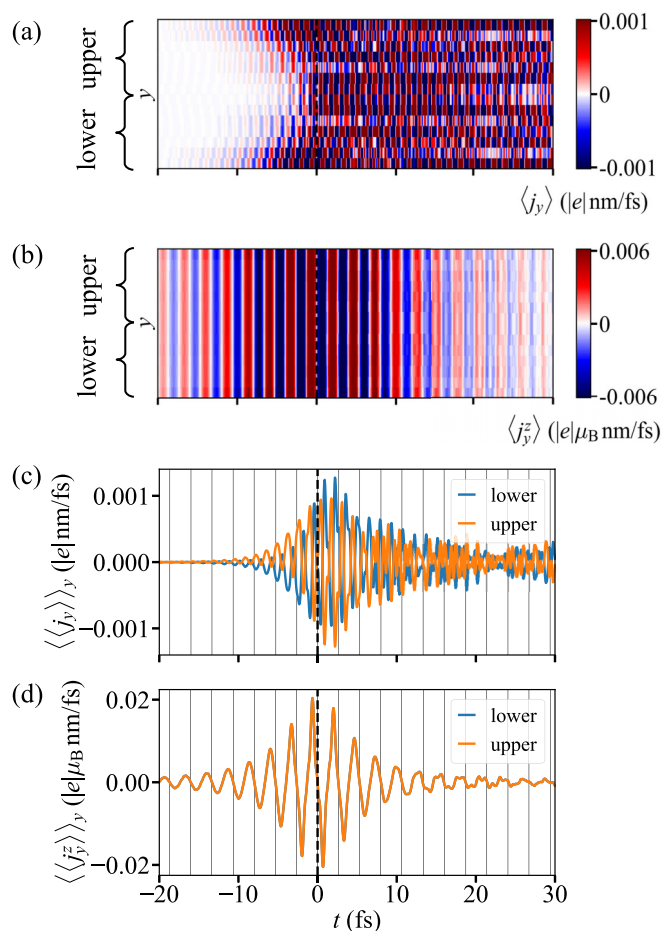
FIG. 3. Transversal currents. (a) Profile of transversal currents depicted as color scale. (b) As panel (a) but for the L^z-polarized OAM currents. (c) and (d) display the data of (a) and (b), respectively, but averaged over the two y regions indicated in panel (a). In panel (d), data for the lower and the upper y region are identical. Vertical lines indicate maxima of the laser's amplitude.

Hamiltonian; these account for the velocities of currents [35]. And third, the inhomogeneous occupation across the ribbon becomes enhanced by the laser-induced dipole transitions, which are stronger the larger the amplitude. The inhomogeneity is clearly seen in the current profile, e.g., at $t > 4$ fs in Fig. 2(c).

IV. LASER-INDUCED TRANSVERSAL CURRENTS

After the analysis of the longitudinal response (along x direction), we turn now to the transverse response (along y direction). The longitudinal currents are accompanied by transversal currents (along the y direction). Initiated at the edges, an antisymmetric spatiotemporal profile evolves [Fig. 3(a)], which develops into a complicated pattern at $t > 0$ fs. For example, the currents in either of the halves (upper/lower regions) do not flow in *one* but in *opposite* directions at a specified time. In other words, the transverse currents mainly compensate each other in the interior of the ribbon, but not at the edges. This results in accumulation of charge at the edges as will be demonstrated below. Note

that in a closed circuit geometry (without edges) the transverse currents compensate everywhere (see Appendix F). In this scenario, one is concerned with a so-called pure OHE, that is, transversal transport of OAM without net charge transport. This finding is in full analogy to a pure spin Hall effect [7].

In order to corroborate the OHE "metaphor" sketched as bent arrows in Fig. 1, we average the transversal currents over the upper and lower regions. As a result, electrons flow on average from the center toward the ribbon edges or vice versa [Fig. 3(c)]. Moreover, they oscillate with half a period of the laser's (e.g., at $t < 0$ fs): regardless of the orientation of the electric field, electrons moving along the ribbon are "deflected" toward the edges. In one half cycle of the laser pulse, however, positive OAM is transported toward the upper edge [Fig. 1(a)], in the next half cycle toward the lower edge [Fig. 1(b)]: the transverse OAM current follows the period of the laser pulse, as seen in Figs. 3(d) and 5.

Besides its period, the region-averaged transversal current differs from its OAM companion within more aspects (snapshots of the orbital dynamics for a full period of the laser pulse are displayed in Appendix E). The OAM current appears much more "regular"; in particular, it is homogeneous across the sample and exhibits a clear-cut time signature, while the current does not [compare Figs. 3(a) and 3(b)]. It is sizable only during the pulse, in contrast to the current which "persists" after the pulse [compare Figs. 3(c) and 3(d) at $t \approx 25$ fs]. They have in common that their extrema do not coincide with those of the laser amplitude; there is a time difference of about $T/4$.

The transverse orbital currents are laser driven: they oscillate periodically with the electric field's frequency. Like for a driven harmonic oscillator, a phase difference of $\pi/2$ occurs, i.e., the OAM current is maximum when the field is zero, and vice versa (see Appendix G). These driven oscillations show up everywhere in the sample, giving rise to an almost homogeneous orbital-current profile [as seen in Figs. 3(b) and 5]. Since the orbital transport is dominated by p electrons, it can be analyzed by means of a two-current model, in which states with $\langle L^z \rangle > 0$ and $\langle L^z \rangle < 0$ are treated separately. These states generate opposite OAM and transversal charge currents, but the same transversal OAM currents at each lattice site. Therefore, only the OAM currents do not vanish in the bulk. In a nanoribbon, the OAM currents lead to accumulation of OAM at the edges. The latter break the inversion symmetry of the bulk, with the consequence that charge currents are initiated at the edges [Fig. 3(a)]. Because there is no relaxation mechanism in the simulations, they persist after the pulse, which leads to complicated spatiotemporal patterns. In contrast, OAM currents can decay due to transitions between the two types of states ($\langle L^z \rangle \lessgtr 0$), which explains that the OAM currents do not persist.

V. LASER-INDUCED OAM AND OCCUPATION

In order to discuss accumulation of OAM at the ribbon's edges, we present occupation $\langle \Delta p_k \rangle$ (i.e., the change of occupation with respect to equilibrium) and OAM $\langle L^z_k \rangle$ [Figs. 4(a) and 4(b)] with a spatiotemporal distribution in analogy to Figs. 3(a) and 3(b). Both quantities are largest (in absolute
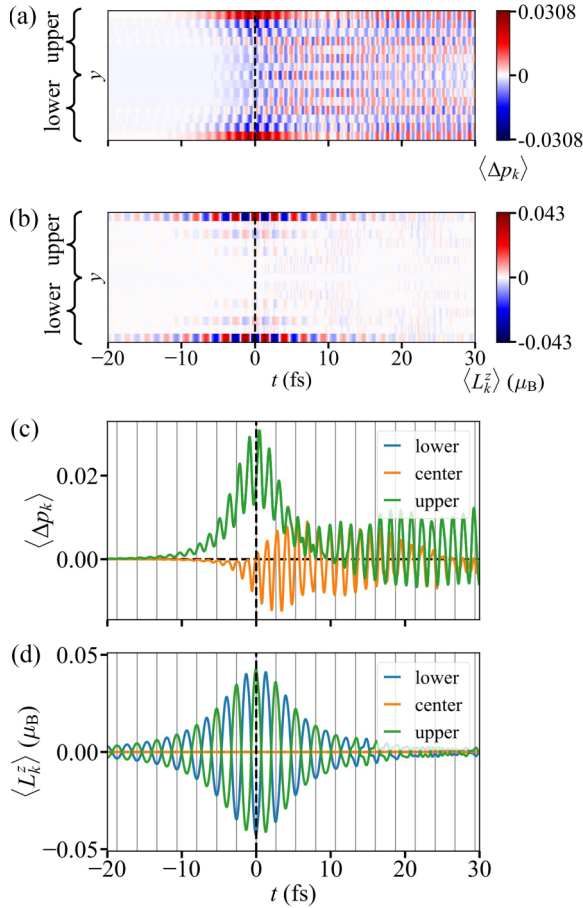
FIG. 4. Accumulation of occupation and orbital angular momentum. (a) Spatiotemporal distribution of occupation change $\langle \Delta p_k \rangle$ relative to the equilibrium distribution across the ribbon width [analogous to Fig. 3(a)]. (b) As panel (a), but for the z component $\langle L_k^z \rangle$ of the OAM. The color bars indicate positive and negative values in red and blue, respectively. (c) As panel (a), but $\langle \Delta p_k \rangle$ vs time t for two edge sites (blue, lower edge; green, upper edge) and a central site (orange). Both edges have identical occupation [as seen in panel (a)] so that the blue spectrum is covered by the green one. (d) As panel (c) but for $\langle L_k^z \rangle$. Opposite edges exhibit OAM with opposite signs. Vertical lines mark the maxima of the laser's amplitude.

value) at edge sites and exhibit significantly smaller values in the sample's interior. In particular L^z is strongly localized at edge sites, exhibiting an absolute value as large as about $0.05 \, \mu_B$ [Figs. 4(b) and 6]. The nonzero $\langle L^z \rangle$ is to a large extent due to hybridization of p_x and p_y orbitals, with minute contributions from $d_{x^2-y^2}$ and d_{xy} orbitals.

In accordance with the antisymmetry of the transversal-current profile [Figs. 3(a) and 3(c)], both edges are identically populated, which corresponds to charge accumulation at the edges [red in Fig. 4(a); there is no Hall voltage], and show half the laser's oscillation period [see Fig. 3(c)]. Closer inspection shows a small time lag with respect to the laser amplitude. More specifically, the extrema of the occupation of the edge sites and a central site are slightly out of phase, which is explained by the finite velocity (determined by the hoppings) of the transversal flow.

A gradient at a sample's edge can result in spin accumulation [55]. In our paper, a gradient is introduced by the nanoribbon's finite extension in y direction. The OAM accumulation can thus be attributed to this gradient. The latter is dominant at the outermost atomic rows, as is the accumulated OAM [Fig. 4(b)].

As has been briefly addressed, the edge occupation comprises L^z-unpolarized and -polarized contributions. Only the latter lead to accumulation of OAM. The OAM time series exhibits opposite signs [Fig. 4(d)], in line with the oppositely L^z-polarized transversal flow [Fig. 3(b)], a finding supporting the oppositely oriented L^z arrows in Fig. 1.

The ultrafast OHE cannot be understood as a time series of steady orbital Hall effects for varying electric field. In a closed circuit geometry, where no accumulation of OAM is possible, we still observe the same phase shifts between laser and orbital current in contrast to a steady orbital Hall effect where j_L is proportional to E (see Fig. 1). Instead, it is laser driven: A maximum orbital current is present when the E field is zero akin to a driven harmonic oscillator which exhibits the same phase relations between driving force and velocity [cf. Figs. 2(a), 3(d), 5, and 10].

VI. CONCLUDING REMARKS

Our detailed theoretical analysis establishes an extension of the well-known static orbital Hall effect onto ultrashort timescales. On the one hand, it fully supports the pictorial presentation of the OHE (Fig. 1). On the other hand, we point out differences between OAM-carrying and non-OAM-carrying quantities, such as OAM currents and (charge) currents. Additionally, the UOHE exhibits specific phase relations between accumulated OAM, OAM currents, and the electric field of the laser. This finding strongly suggests that the UOHE is actually laser driven and not a chronology of steady orbital Hall effects, with each "snapshot" taken for the respective electric field (see Appendix E). Furthermore, since the OHE has been analyzed with an oscillating field, we can observe both OAM currents and the accumulation of OAM. In a static OHE, only one quantity can be analyzed, depending on the considered boundary conditions.

Having established the basics of the ultrafast orbital Hall effect, we are planning to address its dependencies on relevant parameters, for example on details of the laser pulse. Since experimental samples may not be perfect, it is worth investigating imperfections, such as defects or rough edges of the nanoribbon [56], as well as thicker samples.

Our results for Cu nanoribbons call for studies of other materials. As has been shown in Ref. [57] the OHE is larger than the SHE in most metals. It is also worth investigating ferromagnets, where a comparison of ultrafast anomalous, spin, and orbital Hall effects comes to mind. In a recent experiment on ferromagnet/normal metal heterostructures excited by femtosecond laser pulses, terahertz emission spectroscopy was utilized to identify OAM currents [58].

APPENDIX A: ULTRAFAST ELECTRON DYNAMICS

The samples are free-standing fcc(001) monolayers of 15 atomic rows width ("across the ribbon"). These layers form a square lattice, with Cartesian axes chosen as $x \equiv [110]$, $y \equiv [\bar{1}10]$, and $z \equiv [001]$. We apply periodic boundary conditions in x direction (i.e., closed circuit "along the ribbon").

The electronic structure of the samples is described by a tight-binding Hamiltonian

$$\hat{H}_0 = \sum_{k\alpha\sigma} |k\alpha\sigma\rangle \epsilon_{k\alpha\sigma} \langle k\alpha\sigma| + \sum_{k\neq l} \sum_{\alpha\sigma\beta\sigma'} |k\alpha\sigma\rangle t_{k\alpha\sigma,l\beta\sigma'} \langle l\beta\sigma'| \tag{A1}$$

of the cluster in real space, expressed in terms of spin-dependent ($\sigma, \sigma' = \uparrow, \downarrow$) orbitals ($\alpha$ and β index all s, p, and d orbitals of Cu) located at the sites (k, l). The onsite energies $\epsilon_{k\alpha\sigma}$ and the hopping energies $t_{k\alpha\sigma,l\beta\sigma'}$ are parametrized according to the Slater-Koster scheme [40], with numerical values for Cu taken from Ref. [41]. For Cu, we take into account hopping matrix elements for nearest and second-nearest neighbor sites. Moreover, spin-orbit coupling is included following Konschuh *et al.* [42]. The eigenstates

$$|n\rangle = \sum_{k\alpha\sigma} |k\alpha\sigma\rangle c_{k\alpha\sigma,n} \tag{A2}$$

of $\hat{H}_0$ are thus expressed in the site-orbital-spin basis.

The electron system is excited by a femtosecond laser pulse with photon energy $E_{\text{ph}} = \hbar\omega$. In the present paper, the electromagnetic radiation impinges along the z axis onto the ribbon (see Fig. 1), and the azimuth of incidence is chosen such that the electric field oscillates along the x axis. Hence, the laser's electric field is written as

$$\boldsymbol{E}(t) = E_0\, l(t) \cos(\omega t)\, \boldsymbol{e}_x. \tag{A3}$$

Here, $l(t)$ is a Lorentzian envelope, E_0 is the amplitude, and $\boldsymbol{e}_x$ is the unit vector in x direction. The pulse shape $l(t)\cos(\omega t)$ sets the timeframe of the simulations and is thus shown schematically in Fig. 2(a).

The electron dynamics is described by the von Neumann equation

$$-i\hbar \frac{d\hat{\rho}(t)}{dt} = [\hat{\rho}(t), \hat{H}(t)] \tag{A4}$$

for the one-particle density matrix

$$\hat{\rho}(t) = \sum_{n,m} |n\rangle\, p_{nm}(t)\, \langle m|. \tag{A5}$$

$\{|n\rangle\}$ is the set of eigenstates of $\hat{H}_0$, with $\hat{H}_0|n\rangle = \epsilon_n|n\rangle$ [see Eq. (A2)]. The time-dependent Hamiltonian $\hat{H}(t)$ comprises the electric field of the laser via minimal coupling [43] (see below). The equation of motion (A4) for $\hat{\rho}(t)$ is solved within our theoretical framework EVOLVE; for details see Ref. [35].

APPENDIX B: COUPLING ELECTRONS TO THE LASER'S ELECTRIC FIELD

The coupling of a charged particle to an electromagnetic field is achieved by the Peierls substitution

$$\hat{\boldsymbol{p}} \mapsto \hat{\boldsymbol{p}} - \frac{q}{c}\boldsymbol{A}(\boldsymbol{r}, t). \tag{B1}$$

q is the charge of the particle (for an electron $q = -e$), c is the speed of light, and $\boldsymbol{A}(\boldsymbol{r}, t)$ is the vector potential of the electromagnetic field. In what follows we rely on the relation [43]

$$e^{if(x)}\, g(x, \tilde{p})\, e^{-if(x)} = g(x, \tilde{p} - \partial_x f(x)). \tag{B2}$$

Here, $\tilde{p} = -i\partial/\partial x = \hat{p}/\hbar$. Neglecting the effect of the magnetic field associated with the electromagnetic field, we define the scalar function $\chi(\boldsymbol{r}, t)$ by

$$\nabla \chi(\boldsymbol{r}, t) \equiv \boldsymbol{A}(\boldsymbol{r}, t). \tag{B3}$$

The vector potential is assumed spatially constant. Then

$$\chi(\boldsymbol{r}, t) = \boldsymbol{A}_0(t) \cdot \boldsymbol{r}, \tag{B4}$$

that is the dipole operator in length form [59]. Taking

$$f = \frac{q}{c\hbar}\chi \tag{B5}$$

in Eq. (B2), the Peierls substitution can be replaced by a unitary transformation of the unperturbed Hamiltonian $\hat{H}_0(\boldsymbol{r}, \hat{\boldsymbol{p}})$ [43]:

$$\hat{H}(\boldsymbol{r}, \hat{\boldsymbol{p}}, t) = \hat{U}(\boldsymbol{r}, t)\, \hat{H}_0(\boldsymbol{r}, \hat{\boldsymbol{p}})\, \hat{U}^\dagger(\boldsymbol{r}, t) \tag{B6}$$

with

$$\hat{U}(\boldsymbol{r}, t) = \exp\left(\frac{iq}{c\hbar}\chi(\boldsymbol{r}, t)\right). \tag{B7}$$

The unperturbed Hamiltonian reads in second quantization for the eigenstate basis

$$\hat{H}_0 = \sum_{n,m} \hat{c}_n^\dagger\, h_{nm}^{(0)}\, \hat{c}_m, \tag{B8}$$

with

$$h_{nm}^{(0)} = \langle\phi_n|\hat{h}_0|\phi_m\rangle \tag{B9a}$$

$$= \int \phi_n^\star(\boldsymbol{r})\left(\frac{\hat{\boldsymbol{p}}^2}{2m} + V(\boldsymbol{r})\right)\phi_m(\boldsymbol{r})\, dr^3. \tag{B9b}$$

Applying the unitary transformation yields the Hamiltonian with coupling to the electromagnetic field:

$$\hat{H}(t) = \sum_{n,m} \hat{c}_n^\dagger\langle\phi_n|\hat{U}\,\hat{h}_0\,\hat{U}^\dagger|\phi_m\rangle\, \hat{c}_m. \tag{B10}$$

The matrix elements depend on time via the unitary operators. Inserting unit operators

$$\hat{1} = \sum_n |\phi_n\rangle\langle\phi_n| \tag{B11}$$

and expanding the unitary operators up to first order in χ,

$$\hat{U}(\boldsymbol{r}, t) \approx \hat{1} + \frac{iq}{c\hbar}\chi(\boldsymbol{r}, t), \tag{B12}$$

the matrix elements become

$$\langle\phi_n|\hat{U}|\phi_k\rangle \approx \langle\phi_n|\hat{1}|\phi_k\rangle + \frac{iq}{c\hbar}\langle\phi_n|\chi|\phi_k\rangle \tag{B13a}$$

$$= \delta_{nk} + \frac{iq}{c\hbar}\chi_{nk}, \tag{B13b}$$

and similarly for $\hat{U}^{\dagger}(\boldsymbol{r}, t)$. With this follows

$$
\begin{aligned}
\hat{H}(t) \approx & \sum_{n,m} \hat{c}_n^{\dagger} h_{nm}^{(0)} \hat{c}_m \\
& - \frac{iq}{c\hbar} \sum_{n,m,l} \hat{c}_n^{\dagger} h_{nl}^{(0)} \chi_{ml}^{\star} \hat{c}_m + \frac{iq}{c\hbar} \sum_{n,m,l} \hat{c}_n^{\dagger} \chi_{nl} h_{lm}^{(0)} \hat{c}_m \\
& + \left(\frac{q}{c\hbar}\right)^2 \sum_{n,m} \sum_{k,l} \hat{c}_n^{\dagger} \chi_{nk} h_{kl}^{(0)} \chi_{ml}^{\star} \hat{c}_m.
\end{aligned}
\tag{B14}
$$

The matrix elements $h_{nm}^{(0)}$ of the unperturbed Hamiltonian are thus transformed according to

$$
\begin{aligned}
h_{nm}^{(0)} \mapsto & h_{nm}^{(0)} - \frac{iq}{c\hbar} \sum_l h_{nl}^{(0)} \chi_{ml}^{\star} + \frac{iq}{c\hbar} \sum_l \chi_{nl} h_{lm}^{(0)} \\
& + \left(\frac{q}{c\hbar}\right)^2 \sum_{k,l} \chi_{nk} h_{kl}^{(0)} \chi_{ml}^{\star}.
\end{aligned}
\tag{B15}
$$

With the matrix X defined by

$$
(\mathsf{X})_{nl} = \chi_{nl}
\tag{B16}
$$

and the Hamilton matrix

$$
(\mathsf{H}_0)_{lm} = h_{lm}^{(0)}
\tag{B17}
$$

this result yields the matrix

$$
\begin{aligned}
\mathsf{H}(t) \approx & \mathsf{H}_0 - \frac{iq}{c\hbar} \mathsf{H}_0 \mathsf{X}^{\dagger}(t) + \frac{iq}{c\hbar} \mathsf{X}(t) \mathsf{H}_0 \\
& + \left(\frac{q}{c\hbar}\right)^2 \mathsf{X}(t) \mathsf{H}_0 \mathsf{X}^{\dagger}(t)
\end{aligned}
\tag{B18}
$$

of the time-dependent Hamiltonian that enters the von Neumann equation (A4) with the last term being neglected.

APPENDIX C: ORBITAL ANGULAR MOMENTUM CURRENTS

Similarly to the currents of spin angular momentum [37], currents of OAM are derived from the symmetrized expression

$$
\langle j_{kl}^{\mu} \rangle(t) \equiv \frac{1}{2} \left[\langle L_k^{\mu} j_{kl} \rangle(t) + \langle j_{kl} L_l^{\mu} \rangle(t) \right],
\tag{C1}
$$

($\mu = x, y, z$; see for example Refs. [60,61]), in which the operator $\hat{\jmath}_{kl}$ for the current from site l to site k is adapted from Mahan's expression [45]. Using a tight-binding approach for the electronic structure, the one-particle density matrix and the Hamiltonian are given in matrix form. Both are represented in a site-orbital-spin basis $\{|k\alpha\sigma\rangle\}$ (k site index, α orbital, $\sigma = \uparrow, \downarrow$ spin orientation with respect to the z axis). This allows us to define block matrices

$$
\left(\mathsf{p}_{kl}^{\sigma\sigma'}\right)_{\alpha\beta} = p_{k\alpha\sigma, l\beta\sigma'}, \quad \left(\mathsf{t}_{kl}^{\sigma\sigma'}\right)_{\alpha\beta} = t_{k\alpha\sigma, l\beta\sigma'}
\tag{C2}
$$

that are indexed with respect to site and spin. These are further combined into site-indexed 2×2 block matrices:

$$
\mathsf{P}_{lk} = \begin{pmatrix} \mathsf{p}_{lk}^{\uparrow\uparrow} & \mathsf{p}_{lk}^{\uparrow\downarrow} \\ \mathsf{p}_{lk}^{\downarrow\uparrow} & \mathsf{p}_{lk}^{\downarrow\downarrow} \end{pmatrix}, \quad \mathsf{T}_{kl} = \begin{pmatrix} \mathsf{t}_{kl}^{\uparrow\uparrow} & \mathsf{t}_{kl}^{\uparrow\downarrow} \\ \mathsf{t}_{kl}^{\downarrow\uparrow} & \mathsf{t}_{kl}^{\downarrow\downarrow} \end{pmatrix}.
\tag{C3}
$$

With this, Eq. (C1) can be written as

$$
\langle j_{kl}^{\mu} \rangle = -\frac{i}{4} \operatorname{tr} \mathsf{P}_{lk} \left[\mathsf{L}_k^{\mu} \mathsf{T}_{kl} + \mathsf{T}_{kl} \mathsf{L}_l^{\mu} \right] - \langle l \leftrightarrow k \rangle.
\tag{C4}
$$

The μth component ($\mu = x, y, z$) of the OAM operator appears as matrices

$$
\mathsf{L}_m^{\mu} = \begin{pmatrix} \mathsf{l}_m^{\mu} & 0 \\ 0 & \mathsf{l}_m^{\mu} \end{pmatrix},
\tag{C5}
$$

which are diagonal with respect to both site and spin, but depend on the atomic species at site m. Hence, L_m^{μ} in Eq. (C4) is taken either at $m = k$ or at $m = l$. Explicit forms of L_m^{μ} for cubic harmonics can be found for example in Refs. [27,62].

With the above definitions and by exploiting the hermiticity of the matrices as well as the invariance of the trace upon cyclic permutations Eq. (C4) can be written in block-matrix form as

$$
\langle j_{kl}^{\mu} \rangle = \frac{1}{2} \operatorname{Im} \sum_{\sigma,\sigma'} \operatorname{tr} \mathsf{p}_{lk}^{\sigma\sigma'} \left(\mathsf{l}_k^{\mu} \mathsf{t}_{kl}^{\sigma'\sigma} + \mathsf{t}_{kl}^{\sigma'\sigma} \mathsf{l}_l^{\mu} \right).
\tag{C6}
$$

The probability current can be obtained from this expression by setting $\mathsf{l}_k^{\mu} = \mathsf{l}_l^{\mu} = 1$:

$$
\langle j_{kl} \rangle = \operatorname{Im} \sum_{\sigma,\sigma'} \operatorname{tr} \mathsf{p}_{lk}^{\sigma\sigma'} \mathsf{t}_{kl}^{\sigma'\sigma}.
\tag{C7}
$$

Hence, the OAM current $\langle j_{kl}^{\mu} \rangle$ appears as probability current $\langle j_{kl} \rangle$ projected (via l_k^{μ}) onto the OAM-carrying orbital combinations. This is analogous to expectation values $\langle O \rangle_k = \operatorname{Tr}_k(\hat{\rho} \hat{O})$ taken for site k, with $\hat{O} = \hat{1}$ for the occupation probability and $\hat{O} = \hat{L}$ for the OAM.

The currents obey the symmetries $\langle j_{kl} \rangle = -\langle j_{lk} \rangle$ and $\langle j_{kl}^{\mu} \rangle = -\langle j_{lk}^{\mu} \rangle = -\langle j_{kl}^{-\mu} \rangle$. Moreover, they fulfill Kirchhoff's rules, as has been checked in numerical simulations. We focus on nonequilibrium currents, i.e., more precisely on the laser-induced changes with respect to equilibrium currents [60,63–65] that may exist before the laser excitation.

In experiments, edges might not be perfect, for example corrugated. This roughness can be modeled in EVOLVE by removing or replacing atoms. We expect that electrons propagating along the nanoribbon are scattered, thereby altering both longitudinal and transversal currents with respect to a ribbon with perfect edges. This could lead to less homogeneous or less coherent occupation and current profiles.

APPENDIX D: SYMMETRY ANALYSIS

Instead of a full group-theoretical analysis [44], we perform a symmetry analysis which tells what components of the laser-induced OAM are forbidden for the given setup.

The electric field $\boldsymbol{E}$ of the laser is oriented along the x direction. Thus, for the chosen nanoribbon, symmetries that leave E and the ribbon invariant are the reflection $\hat{m}_y$ at the xz plane, $(x, y, z) \rightarrow (x, -y, z)$, and the π rotation $\hat{C}_{2x}$, $(x, y, z) \rightarrow (x, -y, -z)$, about the central line along the nanoribbon (denoted as the x axis here).

Since we are interested in accumulation of OAM at the ribbon's edges, the OAM is decomposed into two regions of the nanoribbon, one with $y < 0$ ("lower," l) and the other with $y > 0$ ("upper," u). Both symmetry operations interchange the edges, that is, l $\leftrightarrow$ u.

Inspection of Table I tells us immediately that $L_l^x = -L_u^x = L_u^x$ (second column) and $L_u^x = -L_l^x = L_l^x$ (fifth column), which can only be fulfilled by $L_l^x = L_u^x = 0$. Likewise

TABLE I. Effect of symmetry operations (left column) components L_r^μ of the orbital angular momentum in the lower region ($r = l$) and in the upper ($r = u$) of the nanoribbon ($\mu = x, y, z$); $\hat{1}$ is the identity operation, and $\hat{m}_y$ and $\hat{C}_{2x}$ are defined in the text.

	L_1^x	L_1^y	L_1^z	L_u^x	L_u^y	L_u^z
$\hat{1}$	L_1^x	L_1^y	L_1^z	L_u^x	L_u^y	L_u^z
$\hat{m}_y$	$-L_u^x$	L_u^y	$-L_u^z$	$-L_1^x$	L_1^y	$-L_1^z$
$\hat{C}_{2x}$	L_u^x	$-L_u^y$	$-L_u^z$	L_1^x	$-L_1^y$	$-L_1^z$

one finds $L_1^y = L_u^y = -L_u^y$ (third column) and $L_u^y = L_1^y = -L_1^y$ (sixth column), implying $L_1^y = L_u^y = 0$. For the z component, however, we arrive at $L_1^z = -L_u^z$ (fourth and seventh column).

In summary, L^x and L^y vanish in the entire ribbon. In contrast, L^z is allowed to be nonzero but antisymmetric ($L_1^z = -L_u^z$) with respect to the central x line of the nanoribbon; this means that the OAM in both regions cancel each other. These symmetries are fully confirmed in the simulations.

Linearly polarized light leads to orbital selection in the excitation (or deexcitation) process via the selection rules for dipole transitions ($\Delta l = \pm 1$; $\Delta m = -1, 0, +1$; $\Delta \sigma = 0$). In the present paper, the electric field along x is even under the reflection $\hat{m}_y$ at the xz plane and, thus, allows only for transitions between even orbitals (e.g., $s \rightarrow p_x$) or between odd orbitals (e.g., $p_y \rightarrow d_{xy}$). The resulting imbalance of orbital occupation together with orbital hybridization can produce a nonzero L^z; circular polarization, which could produce both spin and orbital angular momentum (inverse Faraday effect [66–68]) as well, is therefore dispensable. As briefly mentioned in the main text, we also performed simulations for Cu without spin-orbit coupling which also produced nonzero L^z, corroborating orbital hybridization instead of spin-orbit coupling as origin for the photoinduced OAM which is in agreement with the findings of Go *et al.* [27].

We take the opportunity to add a note on Figs. 4(a) and 4(b) of the main text. The spatiotemporal distribution of the site-resolved occupation $\langle p_k \rangle(t)$ shows that occupation, which besides minute edge effects is homogeneously distributed across the ribbon before the laser pulse, is generally increased at the edges and decreased in the ribbon's interior [see Fig. 4(a) at $t \approx 0$ fs]. Subsequently, it exhibits a symmetric, but complex pattern. Likewise, OAM $\langle L_k^z \rangle$ is highly concentrated at the edge sites, as is evident from Fig. 4(b). Its absolute value follows the laser's envelope (here the Lorentzian profile with 10-fs width centered at $t = 0$ fs.)

APPENDIX E: SNAPSHOTS OF THE DYNAMICS

In accordance with the periodic boundary conditions (closed circuit) along the ribbon, all quantities are x-translational invariant. Besides the probability current we find an L^z current in x direction, that is, a longitudinal response to the electric field E. Focusing on transverse responses, the longitudinal OAM current is not discussed in this paper.

The dynamics starting "before the laser pulse" and ending "after the pulse" may be studied by means of the animations included in the Supplemental Material [39]. Here, we briefly discuss the (orbital) dynamics within the laser's period before

its maximum, that is, from $t = -2.7$ to 0 fs. The data represented in Fig. 5 are those used in the main text.

In Fig. 5(a), at $t = -2.7$ fs, that is, one period before the laser's amplitude maximum, the linearly polarized laser's electric field E is oriented along $-x$ direction (orange arrow) and OAM $\pm L^z$ (vertical red and blue arrows, i.e., in $\pm z$ direction) accumulates at the edges of the ribbon. OAM currents are small.

In Fig. 5(b), a quarter period later ($t = -2.1$ fs, $E = 0$), transverse OAM currents $\boldsymbol{j}_L$ transport OAM across the ribbon in $-y$ direction (blue L^z-currents) and the OAM is strongly diminished at the edges.

In Fig. 5(c), the situation half a period later ($t = -1.3$ fs) is similar to that in Fig. 5(a), but the reversed E field (along $+x$) leads to opposite signs of the induced OAM.

In Fig. 5(d), at $t = -0.7$ fs the situation is similar to that in Fig. 5(b). The direction of the OAM currents $\boldsymbol{j}_L$ is reversed.

In Fig. 5(e), one period later ($t = 0$ fs) we find a situation very close to that in Fig. 5(a). The laser's amplitude is maximum.

We take the opportunity to elaborate on transversal currents.

(1) Transversal currents flow irrespective of the orientation of the laser's electric field (here an oscillating field along $+x$ or $-x$ direction), as is sketched in Fig. 1 (see the bent arrows). In a sample without edges (closed circuit, i.e., with periodic boundaries in x and y direction), the currents in $+y$ and in $-y$ direction compensate each other, meaning that there is no net transversal current. This finding has been verified numerically in respective simulations. One is therefore concerned with a "pure" transversal OAM current (pure in the sense that there is a nonzero OAM current $\langle\langle j_y^z \rangle\rangle_y$, but a vanishing net charge current $\langle\langle j_y \rangle\rangle_y$).

(2) A nonzero net transversal current has therefore to be attributed to the presence of edges in the sample. This consideration is corroborated by Fig. 3(a), which shows that the transversal current is initiated at the edges and not in the interior of the nanoribbon.

Combining these two arguments tells that the transversal current is nonzero and oscillates with half the laser's period. This conclusion is supported by the results shown in Figs. 3(a) and 3(c).

The strong accumulation of occupation and the z component of OAM at the edges is shown in Fig. 6. Charge is strongly localized at the outermost sites, exhibiting a symmetric profile across the nanoribbon [cf. Fig. 4(a)]. $\langle L^z \rangle$ is strongly accumulated at the edge as well, but antisymmetrically in accordance with the symmetry analysis in Appendix D; see also Fig. 4(b).

APPENDIX F: SIMULATIONS FOR CLOSED-CIRCUIT GEOMETRY

In order to reveal the effect of the edges of a nanoribbon, we performed simulations for a nanoribbon with closed-circuit geometry (periodic in both x and y direction) and with otherwise identical parameters. Recall that due to the boundary conditions the eigenenergies of the two systems differ slightly from each other, thereby leading to marginally different occupation probabilities. The eye-catching differences
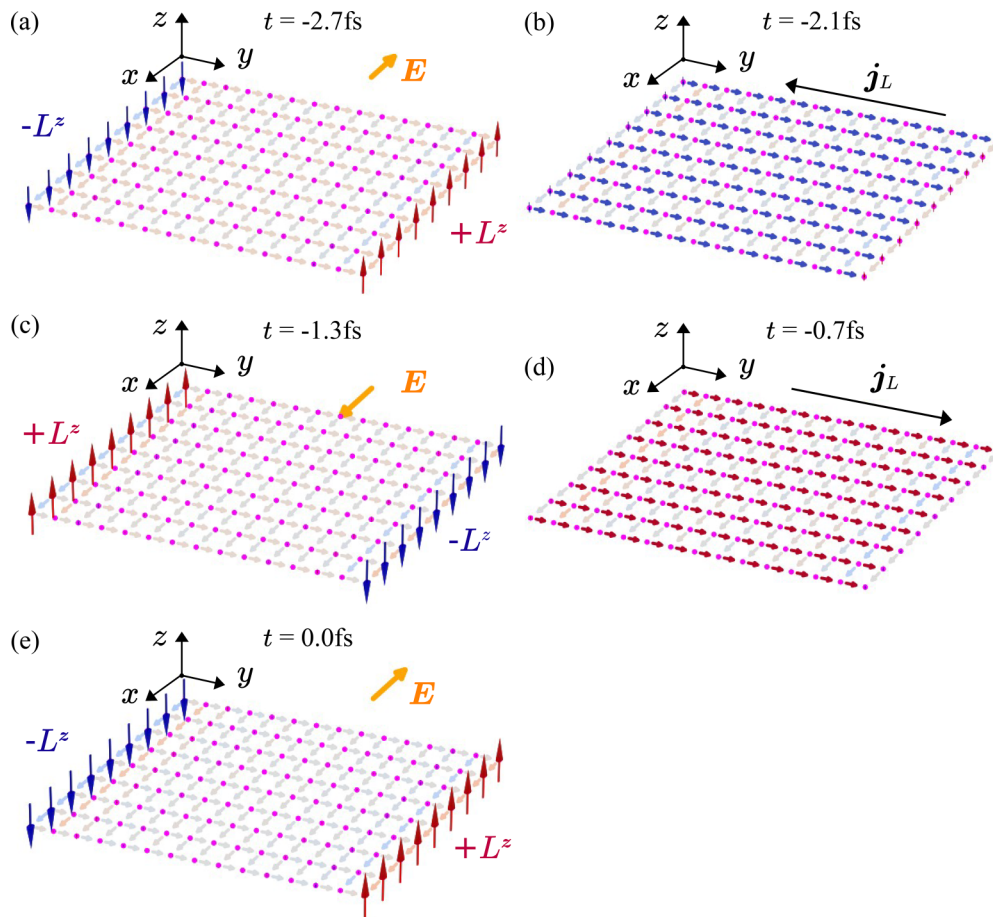
FIG. 5. Snapshots of the orbital angular momentum (OAM) dynamics for a full period of the laser pulse. Small magenta spheres represent the Cu sites on a square lattice [fcc(001) monolayer]. Horizontally oriented small arrows along either $+x$ or $+y$ direction (connecting neighboring Cu atoms) represent the link direction and, thus, the direction of the OAM currents; their color encodes the magnitude and orientation of the L^z-polarized currents (red: positive values; blue: negative values; gray: zero; color saturation: magnitude). (a)–(e) Situations at selected times t (as indicated). Vertically oriented arrows in panels (a), (c), and (e) display the induced OAM (red positive L^z, blue negative L^z.)

in the spatiotemporal patterns discussed below can therefore be clearly attributed to the edges.

The averaged longitudinal currents, compared in Fig. 7 (right column) with their counterparts for the nanoribbon with edges (left column as shown in Fig. 2), follow in both cases the electric field in the beginning of the laser pulse, but show
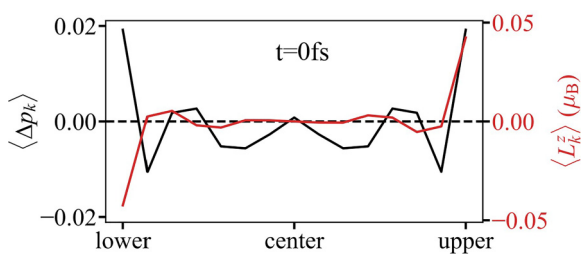

FIG. 6. Accumulation of occupation (black) and $\langle L^z \rangle$ (red) across the nanoribbon at $t = 0$ fs (cf. Fig. 4). $\langle \Delta p_k \rangle$ is the change of occupation with respect to equilibrium (without laser excitation). "Lower," "center," and "upper" indicate the y positions of the edges and the center of the 15 atom wide nanoribbon, respectively.

a slightly different beating pattern afterward [Figs. 7(a) and 7(c)]. The amplitudes are of the same order of magnitude. The edges manifest themselves as a quite complex pattern after the pulse [Fig. 7(b)], whereas the nanoribbon without edges exhibits a pattern of homogeneous streaks [Fig. 7(d)].

As argued in the main text, the nonzero transversal currents are attributed to the presence of the edges, which is proven by the vanishing currents in the ribbon without edges, which are exactly zero [white in Fig. 8(e) as compared to Fig. 8(a)]; see also the y-averaged currents in Figs. 8(c) and 8(g). In contrast, the transversal OAM currents in both nanoribbons are almost identical: they exhibit homogeneous profiles within the entire time span [compare Figs. 8(b) and 8(f)]. The minute differences in the y-averaged OAM currents, in particular after the laser pulse, are attributed to the interference of the longitudinal and transversal currents mediated by the edges [compare Figs. 8(d) and 8(h)]. As for the magnitude of the longitudinal charge currents, those of the transversal OAM currents agree very well.

The above observations support that the OAM currents are driven by the laser and that accumulation is unequivocally an edge effect. Moreover, the main features of the pure ultrafast
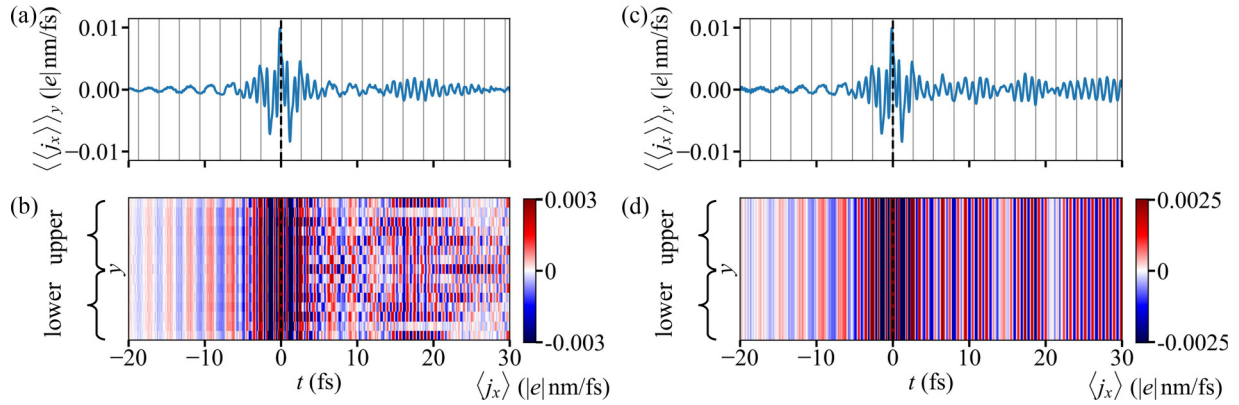
FIG. 7. Longitudinal currents in a nanoribbon with edges (open-circuit geometry, left column with data from Fig. 2) and without edges (closed-circuit geometry, right column). (a), (c) Longitudinal current $\langle\langle j_x\rangle\rangle_y(t)$; see text. Vertical lines mark maxima of the laser amplitude. (b), (d) Profile of currents of x-oriented current filaments (along the ribbon), depicted as color scale. The y average of these currents gives the data shown in the panel above.

OHE for the nanoribbon without edges, namely a transversal OAM current in connection with a vanishing transversal charge current, show up in the ribbon with edges as well. For example, the transversal charge current is initiated at the edges, while it is tiny in the interior of the nanoribbon; see in Fig. 3(a) neither accumulation of charge nor that of OAM.

The double frequency of the transversal charge current [Fig. 3(c)] is explained within a two-current model, in which the two currents transport $+L^z$ and $-L^z$, respectively, besides transporting electric charge. These currents correspond to the red and blue arrows in Fig. 1. Recall that transport of $+L^z$ in one direction is equivalent to transport of $-L^z$ in the opposite direction.
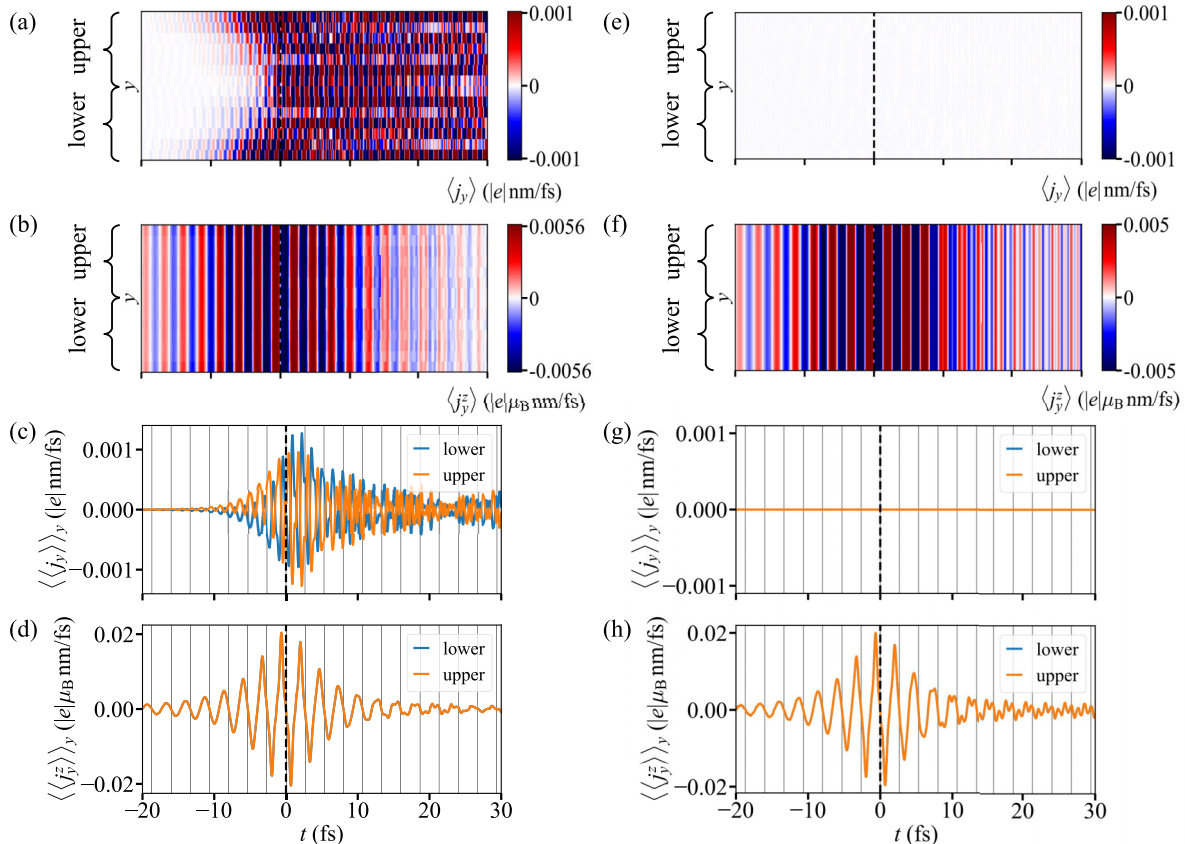

FIG. 8. Transversal currents in a nanoribbon with edges (open-circuit geometry, left column with data from Fig. 3) and without edges (closed-circuit geometry, right column). (a), (e) Profile of transversal currents, depicted as color scale. (b), (f) Respective panel above but for the L^z-polarized OAM currents. (c), (d), (g), (h) Data of (a), (b), (e), and (f), respectively, but averaged over the two upper and lower y regions. In panel (d) and (h), data for the lower and the upper y region are identical. Vertical lines indicate maxima of the laser's amplitude.
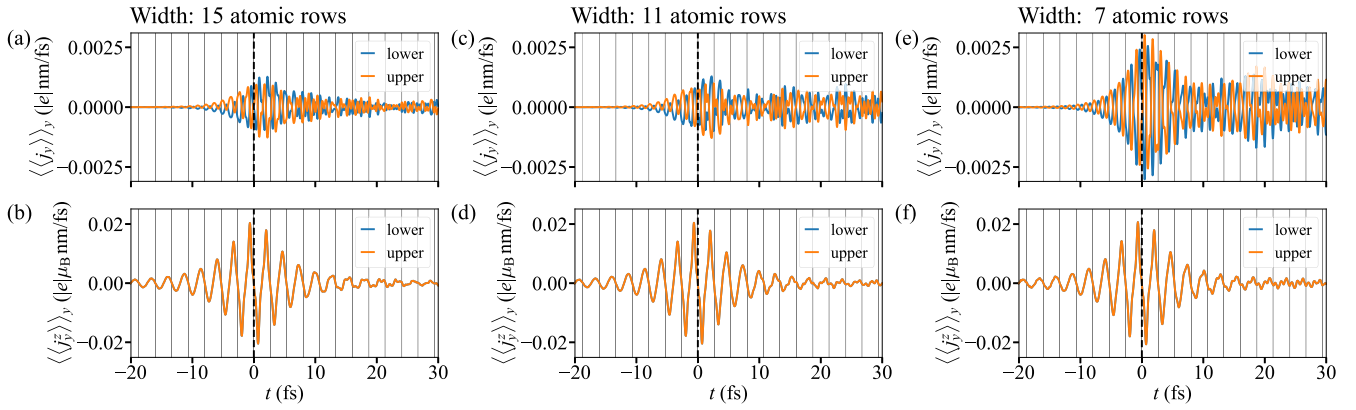
FIG. 9. Dependence of transversal currents on a nanoribbon's width. Top and bottom rows show the charge current and orbital current, respectively, averaged over the upper and lower y regions. Left: Data shown in panels (a) and (b) are taken from Fig. 3 (width of 15 atomic rows). Center and right: As left column but for widths of 11 and 7 atomic rows, respectively. The OAM currents in the lower and the upper y region are identical (cf. bottom row). Vertical lines indicate maxima of the laser's amplitude.

Now suppose that in a closed-circuit geometry the electric field of the laser points in $+x$ direction at a time t [Fig. 8(f)]. There is no net transversal charge current, but a nonzero OAM current [Fig. 8(e)]. This finding is readily explained by the two currents having equal strength but flowing in opposite directions. At time $t + T/2$ the electric field is reversed (T period of the laser radiation). Again there is no net charge current, but the reversed OAM current tells us that the currents transport L^z in opposite directions: their transport directions have been interchanged.

In order to observe a net charge current, symmetry breaking is necessary; this is realized by the nanoribbon with its edges in open-circuit geometry. Before the laser pulse the charge currents still compensate each other in the interior of the nanoribbon [Fig. 8(a)], as for the closed-circuit geometry. The presence of the edges, however, prevents this compensation of the charge currents near the edges. As a result, a transversal charge current gradually "invades" the interior of the nanoribbon [Fig. 8(a)]. It thus modifies the charge currents in such a way that the compensation is destructed but the double frequency is maintained. When the electric field is maximum (along $+x$ direction) and minimum (along $-x$ direction), an uncompensated charge current occurs away from the edge (along $+y$ direction) transporting $+\langle L^z \rangle$ and $-\langle L^z \rangle$, respectively. Therefore, the charge current at the outermost layer has a maximum twice per period while the orbital current has only one. Hence, $\langle j_y \rangle$ oscillates with twice the laser period and is initiated at the edges [Figs. 8(a) and 8(c)], while $\langle j_y^z \rangle$ oscillates with the laser period and is generated in the entire nanoribbon [Figs. 8(d) and 8(h)].

Further simulations for nanoribbons in open-circuit geometry show that prominent features of the transversal currents that have been discussed in Sec. IV (i.e., doubled frequency of $\langle j_y \rangle$, initiation of $\langle j_y \rangle$ at the edges, and homogeneity of $\langle j_y^z \rangle$) are barely affected by the nanoribbon's width (Fig. 9). While the OAM currents are akin, with tiny variations after the laser-pulse maximum (bottom row), the width of a nanoribbon mainly affects the interference pattern of $\langle j_y \rangle$ [as depicted in Fig. 3(a)], which results in the different complex patterns

observed for $t > -2$ fs and the decreasing maximum amplitude with increasing width (top row).

APPENDIX G: CLASSICAL ANALOGY FOR THE LASER-DRIVEN DYNAMICS

Our simulations show that the orbital angular momentum accumulated at the sample's edges is reminiscent of a harmonic function of time t. It is in phase with the electric field of the laser or has a phase shift of π, depending on the considered edge [Fig. 4(d)]. The transverse OAM currents are harmonic as well, but have their maximum a quarter of a period $T/4$ earlier [Fig. 3(d)]. The OAM currents are largest when the electric field vanishes. In addition, the transverse OAM currents exhibit the same phase relations for periodic boundary conditions in y direction, where there are no edges and thus no accumulation, as is found in respective simulations (not shown here).

These findings suggest that the OAM currents are primarily *not* caused by equilibration of the accumulated OAM once the field is reduced or vanishes. Moreover, the time difference of $T/4$ cannot be understood within the scenario of a constant electric field, in which the transverse OAM current would be *proportional to and in phase with* the electric field, as would follow from $j_y^z(t) = \sigma_{yx}^z E_x(t)$ (σ_{yx}^z element of the OAM conductivity tensor).

In order to illuminate the above phenomena, we identify the accumulated OAM with the mechanical displacement $x(t)$ of a driven, damped harmonic oscillator and the OAM currents with its velocity $v(t) = dx(t)/dt$. In the respective Newtonian equation of motion

$$\frac{d^2 x(t)}{dt^2} + 2\xi \omega_0 \frac{dx(t)}{dt} + \omega_0^2 x + A_0 \sin(\omega_d t) = 0, \quad \text{(G1)}$$

ξ and ω_0 are the damping constant and the eigenfrequency of the undamped oscillator, respectively. The driving force with amplitude A_0 is considered harmonic, which allows us to identify it with the electric field of the laser ($A_0 = eE_0/m$). ω_d thus mimics the laser's carrier frequency that is higher than the characteristic frequency of the electron's motion,
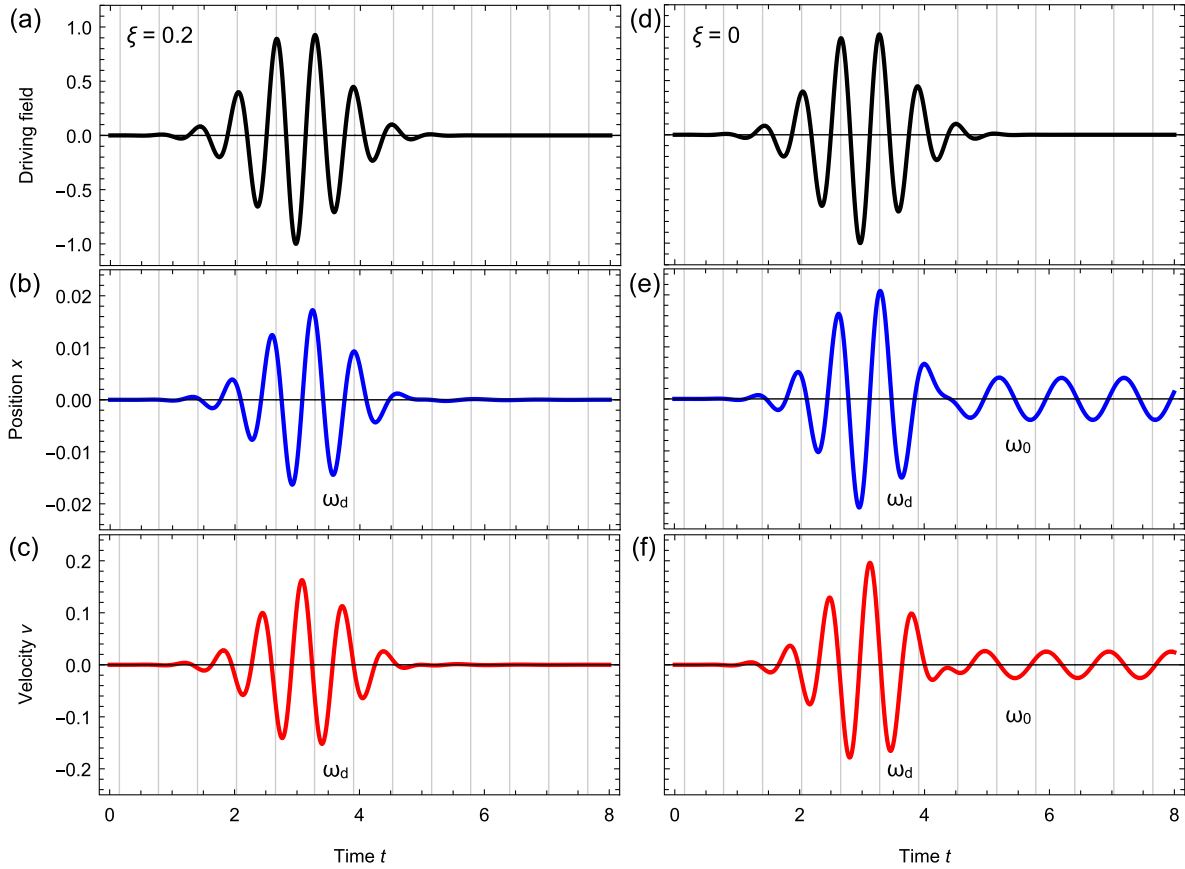
FIG. 10. Driven harmonic oscillator. Left: Panels (a)–(c) depict the amplitude of the driving force, the position $x(t)$, and the velocity $v(t)$ vs time t for the damped case $\xi = 0.2$, respectively. Right: Panels (d)–(f) show the same quantities for the undamped case, $\xi = 0$. The parameters are given in the text.

which translates into $\omega_d \gg \omega_0$. ω_0 defines a characteristic timescale which is determined by the hopping parameters in the tight-binding Hamiltonian. Note that, due to the number of orbitals and lattice sites that are involved in the tight-binding model, several distinct $\omega_{0,i}$ exist in general. For simplicity, the problem is simplified and mapped to a one-dimensional oscillator that is characterized by a single ω_0 in this Appendix.

The complete solution is a superposition of a transient and a steady state. Due to damping, the transient solution becomes negligible at $t \to \infty$. The steady state

$$x(t) = x_0 \sin (\omega_d t + \Delta\phi) \tag{G2}$$

is a harmonic oscillation with frequency ω_d and amplitude

$$x_0 = \frac{A_0}{\omega_d \sqrt{(2\omega_0\xi)^2 + \left(\frac{\omega_d^2 - \omega_0^2}{\omega_d}\right)^2}}. \tag{G3}$$

It is shifted in phase by

$$\Delta\phi = \arctan \left(\frac{2\omega_d\omega_0\xi}{\omega_d^2 - \omega_0^2} \right) \tag{G4}$$

with respect to the driving force. In the limit $\omega_d \gg \omega_0$ this becomes $\Delta\phi \to 0$. Likewise, the velocity

$$v(t) = x_0\omega_d \sin (\omega_d t + \Delta\varphi), \quad \Delta\varphi = \Delta\phi + \pi/2 \tag{G5}$$

is shifted in phase by $\Delta\varphi \to \pi/2$, which translates into a time shift by $T/4$.

A similar behavior is observed when the driving force is not a harmonic function with a constant amplitude but with a Gaussian envelope,

$$A_0 \sin(\omega_d t) \to A_0 \sin(\omega_d t) \, e^{-\left(\frac{t-t'}{t_0}\right)^2}, \tag{G6}$$

as for a laser pulse. An exemplary solution with dimensionless parameters $\xi = 0.2$, $\omega_0 = 2\pi$, $\omega_d = 1.6\,\omega_0$, $t_0 = 1$, $t' = 3$, and $A_0 = 1$ is shown in the left column of Fig. 10. Any transient solution decays immediately and the motion is governed by the driving force [Figs. 10(b) and 10(c)]. The phase shift is as explained above: the velocity is approximately maximum when the driving field is zero.

The OAM and OAM currents can be mapped quite well to this damped and periodically driven harmonic oscillator. This may appear surprising at first glance because we do not account explicitly for "friction" (i.e., a damping mechanism) in the simulations presented in the main text. In the context of OAM, "damping" includes any mechanism that allows us to reduce OAM. Such a mechanism exists due to the off-diagonal hopping terms in the Hamiltonian. Put another way, OAM decays in the same manner it is generated, namely via hybridization of orbitals.

By contrast, charge accumulation and charge currents cannot be mapped onto the model of the damped harmonic oscillator because a respective decay mechanism for charge does not exist in the simulations presented in the main text. Therefore, we now consider a driven, undamped harmonic oscillator ($\xi = 0$, right column of Fig. 10). After the pulse the solution is a harmonic function with the eigenfrequency of the system ω_0, because this mode cannot decay. In the nanoribbon presented in the main text, many such modes with various eigenfrequencies are excited at the edges, giving rise to the fluctuating distribution of transverse charge currents in Fig. 3(a). Such currents are generated by the pulse and

persist indefinitely. By contrast, any oscillations with ω_0 in the OAM currents decay due to the OAM decay mechanism based on orbital hybridization. This is why the transverse OAM currents almost perfectly follow the laser's field [cf. Figs. 2(a) and 3(b)].

We conclude that the analogy of a classical driven harmonic oscillator corroborates the ultrafast electron dynamics, since it exhibits the same phase relations as the OAM and OAM currents with respect to the electric field of the laser [cf. Figs. 2(a) and 3(d)]. Put another way, the ultrafast orbital Hall effect is actually laser driven; it is not a time series of steady orbital Hall effects for varying electric field.

---

[1] Y. Cao, G. Xing, H. Lin, N. Zhang, H. Zheng, and K. Wang, Prospect of spin-orbitronic devices and their applications, iScience **23**, 101614 (2020).

[2] D. Go, D. Jo, H.-W. Lee, M. Kläui, and Y. Mokrousov, Orbitronics: Orbital currents in solids, Europhys. Lett. **135**, 37001 (2021).

[3] T. G. Rappoport, First light on orbitronics as a viable alternative to electronics, Nature **619**, 38 (2023).

[4] M. I. D'yakonov and V. I. Perel, Current-induced spin orientation of electrons in semiconductors, Phys. Lett. A **35**, 459 (1971).

[5] J. E. Hirsch, Spin Hall effect, Phys. Rev. Lett. **83**, 1834 (1999).

[6] Y. K. Kato, R. C. Myers, A. C. Gossard, and D. D. Awschalom, Observation of the spin Hall effect in semiconductors, Science **306**, 1910 (2004).

[7] J. Sinova, S. O. Valenzuela, J. Wunderlich, C. H. Back, and T. Jungwirth, Spin Hall effects, Rev. Mod. Phys. **87**, 1213 (2015).

[8] A. G. Aronov and Y. B. Lyanda-Geller, Nuclear electric resonance and orientation of carrier spins by an electric field, JETP Lett. **50**, 431 (1989).

[9] V. Edelstein, Spin polarization of conduction electrons induced by electric current in two-dimensional asymmetric electron systems, Solid State Commun. **73**, 233 (1990).

[10] J.-I. Inoue, G. E. W. Bauer, and L. W. Molenkamp, Diffuse transport and spin accumulation in a Rashba two-dimensional electron gas, Phys. Rev. B **67**, 033104 (2003).

[11] P. Gambardella and I. M. Miron, Current-induced spin-orbit torques, Phil. Trans. R. Soc. A **369**, 3175 (2011).

[12] S. Zhang and Z. Yang, Intrinsic spin and orbital angular momentum Hall effect, Phys. Rev. Lett. **94**, 066602 (2005).

[13] B. A. Bernevig, T. L. Hughes, and S.-C. Zhang, Orbitronics: The intrinsic orbital current in p-doped silicon, Phys. Rev. Lett. **95**, 066601 (2005).

[14] H. Kontani, T. Tanaka, D. S. Hirashima, K. Yamada, and J. Inoue, Giant intrinsic spin and orbital Hall effects in Sr_2MO_4 (M = Ru, Rh, Mo), Phys. Rev. Lett. **100**, 096601 (2008).

[15] T. Tanaka, H. Kontani, M. Naito, T. Naito, D. S. Hirashima, K. Yamada, and J. Inoue, Intrinsic spin Hall effect and orbital Hall effect in $4d$ and $5d$ transition metals, Phys. Rev. B **77**, 165117 (2008).

[16] H. Kontani, T. Tanaka, D. S. Hirashima, K. Yamada, and J. Inoue, Giant orbital Hall effect in transition metals: Origin of large spin and anomalous Hall effects, Phys. Rev. Lett. **102**, 016601 (2009).

[17] S. Zhong, J. E. Moore, and I. Souza, Gyrotropic magnetic effect and the magnetic moment on the Fermi surface, Phys. Rev. Lett. **116**, 077201 (2016).

[18] T. Yoda, T. Yokoyama, and S. Murakami, Orbital Edelstein effect as a condensed-matter analog of solenoids, Nano Lett. **18**, 916 (2018).

[19] L. Salemi, M. Berritta, A. K. Nandy, and P. M. Oppeneer, Orbitally dominated Rashba-Edelstein effect in noncentrosymmetric antiferromagnets, Nat. Commun. **10**, 5381 (2019).

[20] A. Johansson, B. Göbel, J. Henk, M. Bibes, and I. Mertig, Spin and orbital Edelstein effects in a two-dimensional electron gas: Theory and application to $SrTiO_3$ interfaces, Phys. Rev. Res. **3**, 013275 (2021).

[21] H. A. Hafez, X. Chai, A. Ibrahim, S. Mondal, D. Férachou, X. Ropagnol, and T. Ozaki, Intense terahertz radiation and their applications, J. Opt. **18**, 093004 (2016).

[22] K. C. Phillips, H. H. Gandhi, E. Mazur, and S. K. Sundaram, Ultrafast laser processing of materials: A review, Adv. Opt. Photon. **7**, 684 (2015).

[23] I. Lyalin, S. Alikhah, M. Berritta, P. M. Oppeneer, and R. K. Kawakami, Magneto-optical detection of the orbital Hall effect in chromium, Phys. Rev. Lett. **131**, 156702 (2023).

[24] Y.-G. Choi, D. Jo, K.-H. Ko, D. Go, K.-H. Kim, H. G. Park, C. Kim, B.-C. Min, G.-M. Choi, and H.-W. Lee, Observation of the orbital Hall effect in a light metal Ti, Nature (London) **619**, 52 (2023).

[25] M. Seemann, D. Ködderitzsch, S. Wimmer, and H. Ebert, Symmetry-imposed shape of linear response tensors, Phys. Rev. B **92**, 155138 (2015).

[26] N. Nagaosa, J. Sinova, S. Onoda, A. H. MacDonald, and N. P. Ong, Anomalous Hall effect, Rev. Mod. Phys. **82**, 1539 (2010).

[27] D. Go, D. Jo, C. Kim, and H.-W. Lee, Intrinsic spin and orbital Hall effects from orbital texture, Phys. Rev. Lett. **121**, 086602 (2018).

[28] F. de Juan, A. G. Grushin, T. Morimoto, and J. E. Moore, Quantized circular photogalvanic effect in Weyl semimetals, Nat. Commun. **8**, 15995 (2017).

[29] H. Rostami and M. Polini, Nonlinear anomalous photocurrents in Weyl semimetals, Phys. Rev. B **97**, 195151 (2018).

[30] B. M. Fregoso, Bulk photovoltaic effects in the presence of a static electric field, Phys. Rev. B **100**, 064301 (2019).

[31] J. E. Sipe and A. I. Shkrebtii, Second-order optical response in semiconductors, Phys. Rev. B **61**, 5337 (2000).

[32] H. Xu, J. Zhou, H. Wang, and J. Li, Light-induced static magnetization: Nonlinear Edelstein effect, Phys. Rev. B **103**, 205417 (2021).

[33] T. Adamantopoulos, M. Merte, D. Go, F. Freimuth, S. Blügel, and Y. Mokrousov, Laser-induced charge and spin photocurrents at the BiAg$_2$ surface: A first-principles benchmark, Phys. Rev. Res. **4**, 043046 (2022).

[34] M. Mancini, G. Pagano, G. Cappellini, L. Livi, M. Rider, J. Catani, C. Sias, P. Zoller, M. Inguscio, M. Dalmonte, and L. Fallani, Observation of chiral edge states with neutral fermions in synthetic Hall ribbons, Science **349**, 1510 (2015).

[35] F. Töpler, J. Henk, and I. Mertig, Ultrafast spin dynamics in inhomogeneous systems: A density-matrix approach applied to Co/Cu interfaces, New J. Phys. **23**, 033042 (2021).

[36] F. Ziolkowski, O. Busch, I. Mertig, and J. Henk, Ultrafast spin dynamics: Complementing theoretical analyses by quantum state measures, J. Phys.: Condens. Matter **35**, 125501 (2023).

[37] O. Busch, F. Ziolkowski, I. Mertig, and J. Henk, Ultrafast dynamics of electrons excited by femtosecond laser pulses: Spin polarization and spin-polarized currents, Phys. Rev. B **108**, 184401 (2023).

[38] O. Busch, F. Ziolkowski, I. Mertig, and J. Henk, Ultrafast dynamics of orbital angular momentum of electrons induced by femtosecond laser pulses: Generation and transfer across interfaces, Phys. Rev. B **108**, 104408 (2023).

[39] See Supplemental Material at http://link.aps.org/supplemental/10.1103/PhysRevResearch.6.013208 for animations of the (orbital) dynamics.

[40] J. C. Slater and G. F. Koster, Simplified LCAO method for the periodic potential problem, Phys. Rev. **94**, 1498 (1954).

[41] D. A. Papaconstantopoulos, *Handbook of the Band Structure of Elemental Solids* (Springer-Verlag, Berlin, 2015).

[42] S. Konschuh, M. Gmitra, and J. Fabian, Tight-binding theory of the spin-orbit coupling in graphene, Phys. Rev. B **82**, 245412 (2010).

[43] S. Savasta and R. Girlanda, The particle-photon interaction in systems described by model Hamiltonians in second quantization, Solid State Commun. **96**, 517 (1995).

[44] J. Henk, T. Scheunemann, S. V. Halilov, and R. Feder, Magnetic dichroism and electron spin polarization in photoemission: Analytical results, J. Phys.: Condens. Matter **8**, 47 (1996).

[45] G. D. Mahan, *Many-Particle Physics*, 3rd ed. (Springer, New York, 2000).

[46] A. Pezo, D. García Ovalle, and A. Manchon, Orbital Hall effect in crystals: Interatomic versus intra-atomic contributions, Phys. Rev. B **106**, 104414 (2022).

[47] Focusing on nonequilibrium scenarios, possible equilibrium currents are subtracted. The latter would vanish if angular momentum currents were properly defined; see Refs. [69,70] for a discussion of spin currents. Explicit expressions for the currents are given in Appendix C.

[48] Y. Niimi, M. Morota, D. H. Wei, C. Deranlot, M. Basletic, A. Hamzic, A. Fert, and Y. Otani, Extrinsic spin Hall effect induced by iridium impurities in copper, Phys. Rev. Lett. **106**, 126601 (2011).

[49] S. Ding, A. Ross, D. Go, L. Baldrati, Z. Ren, F. Freimuth, S. Becker, F. Kammerbauer, J. Yang, G. Jakob, Y. Mokrousov, and M. Kläui, Harnessing orbital-to-spin conversion of interfacial orbital currents for efficient spin-orbit torques, Phys. Rev. Lett. **125**, 177201 (2020).

[50] D. Go and H.-W. Lee, Orbital torque: Torque generation by orbital current injection, Phys. Rev. Res. **2**, 013177 (2020).

[51] G. Sala and P. Gambardella, Giant orbital Hall effect and orbital-to-spin conversion in 3d, 5d, and 4f metallic heterostructures, Phys. Rev. Res. **4**, 033037 (2022).

[52] O. Busch, I. Mertig, and B. Göbel, Orbital Hall effect and orbital edge states caused by s electrons, Phys. Rev. Res. **5**, 043052 (2023).

[53] L. M. Canonico, T. P. Cysne, A. Molina-Sanchez, R. B. Muniz, and T. G. Rappoport, Orbital Hall insulating phase in transition metal dichalcogenide monolayers, Phys. Rev. B **101**, 161409(R) (2020).

[54] L. M. Canonico, T. P. Cysne, T. G. Rappoport, and R. B. Muniz, Two-dimensional orbital Hall insulators, Phys. Rev. B **101**, 075429 (2020).

[55] A. Shitade and G. Tatara, Spin accumulation without spin current, Phys. Rev. B **105**, L201202 (2022).

[56] S. Ghosh, F. Freimuth, O. Gomonay, S. Blügel, and Y. Mokrousov, Driving spin chirality by electron dynamics in laser-excited antiferromagnets, Commun. Phys. **5**, 69 (2022).

[57] L. Salemi and P. M. Oppeneer, First-principles theory of intrinsic spin and orbital Hall and Nernst effects in metallic monoatomic crystals, Phys. Rev. Mater. **6**, 095001 (2022).

[58] T. S. Seifert, D. Go, H. Hayashi, R. Rouzegar, F. Freimuth, K. Ando, Y. Mokrousov, and T. Kampfrath, Time-domain observation of ballistic orbital-angular-momentum currents with giant relaxation length in tungsten, Nat. Nanotechnol. **18**, 1132 (2023).

[59] A. F. Starace, Length and velocity formulas in approximate oscillator-strength calculations, Phys. Rev. A **3**, 1242 (1971).

[60] B. K. Nikolić, L. P. Zârbo, and S. Souma, Imaging mesoscopic spin Hall flow: Spatial distribution of local spin currents and spin densities in and out of multiterminal spin-orbit coupled semiconductor nanostructures, Phys. Rev. B **73**, 075303 (2006).

[61] M. D. Petrović, B. S. Popescu, U. Bajpai, P. Plecháč, and B. K. Nikolić, Spin and charge pumping by a steady or pulse-current-driven magnetic domain wall: A self-consistent multiscale time-dependent quantum-classical hybrid approach, Phys. Rev. Appl. **10**, 054038 (2018).

[62] D. Jo, D. Go, and H.-W. Lee, Gigantic intrinsic orbital Hall effects in weakly spin-orbit coupled metals, Phys. Rev. B **98**, 214405 (2018).

[63] E. I. Rashba, Spin currents in thermodynamic equilibrium: The challenge of discerning transport currents, Phys. Rev. B **68**, 241315(R) (2003).

[64] İ. Adagideli, M. Scheid, M. Wimmer, G. E. W. Bauer, and K. Richter, Extracting current-induced spins: Spin boundary conditions at narrow Hall contacts, New J. Phys. **9**, 382 (2007).

[65] I. V. Tokatly, Equilibrium spin currents: Non-Abelian gauge invariance and color diamagnetism in condensed matter, Phys. Rev. Lett. **101**, 106601 (2008).

[66] A. V. Kimel, A. Kirilyuk, P. A. Usachev, R. V. Pisarev, A. M. Balbashov, and T. Rasing, Ultrafast non-thermal control of magnetization by instantaneous photomagnetic pulses, Nature (London) **435**, 655 (2005).

[67] R. Hertel, Theory of the inverse Faraday effect in metals, J. Magn. Magn. Mater. **303**, L1 (2006).

[68] S. B. Mishra and S. Coh, Spin contribution to the inverse Faraday effect of nonmagnetic metals, Phys. Rev. B **107**, 214432 (2023).

[69] Q. F. Sun and X. C. Xie, Definition of the spin current: The angular spin current and its physical consequences, Phys. Rev. B **72**, 245305 (2005).

[70] J. Shi, P. Zhang, D. Xiao, and Q. Niu, Proper definition of spin current in spin-orbit coupled systems, Phys. Rev. Lett. **96**, 076604 (2006).